Superconductor Science and Technology

PAPER • **OPEN ACCESS**

Atomic-scale analyses of Nb_3Sn on Nb prepared by vapor diffusion for superconducting radiofrequency cavity applications: a correlative study

To cite this article: Jaeyel Lee *et al* 2019 *Supercond. Sci. Technol.* **32** 024001

OPEN ACCESS
IOP Publishing
Superconductor Science and Technology
Supercond. Sci. Technol. **32** (2019) 024001 (16pp)
https://doi.org/10.1088/1361-6668/aaf268

Atomic-scale analyses of Nb_3Sn on Nb prepared by vapor diffusion for superconducting radiofrequency cavity applications: a correlative study

Jaeyel Lee[1,2,6], Sam Posen[2,6], Zugang Mao[1], Yulia Trenikhina[2], Kai He[1,3], Daniel L Hall[4], Matthias Liepe[4] and David N Seidman[1,5,6]

[1] Department of Materials Science and Engineering, Northwestern University, Evanston, IL 60208, United States of America
[2] Fermi National Accelerator Laboratory, Batavia, IL 60510, United States of America
[3] Northwestern University Atomic and Nanoscale Characterization Experimental Center (NUANCE), Evanston, IL 60208, United States of America
[4] Cornell Laboratory for Accelerator-Based Sciences and Education, Cornell University, Ithaca, NY 14853, United States of America
[5] Northwestern University Center for Atomic Probe Tomography (NUCAPT), Evanston, IL 60208, United States of America

E-mail: jaeyel.lee@gmail.com, sposen@fnal.gov and d-seidman@northwestern.edu

Received 11 October 2018, revised 8 November 2018
Accepted for publication 20 November 2018
Published 20 December 2018

Abstract

We report on atomic-scale analyses of the microstructure of an Nb_3Sn coating on Nb, prepared by a vapor diffusion process for superconducting radiofrequency (SRF) cavity applications using transmission electron microscopy, electron backscatter diffraction and first-principles calculations. Epitaxial growth of Nb_3Sn on a Nb substrate is found and four types of orientation relationships (ORs) at the Nb_3Sn/Nb interface are identified by electron diffraction or high-resolution scanning transmission electron microscopy (HR-STEM) analyses. Thin Nb_3Sn grains are observed in regions with a low Sn flux and they have a specific OR: Nb_3Sn $(1\bar{2}0)$//Nb $(\bar{1}11)$ and Nb_3Sn (002)//Nb $(0\bar{1}1)$. The Nb_3Sn/Nb interface of thin grains has a large lattice mismatch, 12.3%, between Nb $(0\bar{1}1)$ and Nb_3Sn (002) and a high density of misfit dislocations as observed by HR-STEM. Based on our microstructural analyses of the thin grains, we conclude that the thin regions are probably a result of a slow interfacial migration with this particular OR. The Sn-deficient regions are seen to form initially at the Nb_3Sn/Nb interface and remain in the grains due to the slow diffusion of Sn in bulk Nb_3Sn. The formation of Sn-deficient regions and the effects of interfacial energies on the formation of Sn-deficient regions at different interfaces are estimated by first-principles calculations. The finding of ORs at the Nb_3Sn/Nb interface provides important information about the formation of imperfections in Nb_3Sn coatings, such as large thin-regions and Sn-deficient regions, which are critical to the performance of Nb_3Sn SRF cavities for accelerators.

[6] Authors to whom any correspondence should be addressed.

Supplementary material for this article is available online

Keywords: Nb_3Sn, defects, orientation relationship, superconducting radiofrequency cavity, transmission electron microscopy

(Some figures may appear in colour only in the online journal)

1. Introduction

Nb_3Sn is an A15-type superconductor, which has been actively studied and used in superconducting wire applications [1]. A number of studies have employed Nb_3Sn coatings on Nb for superconducting radiofrequency (SRF) cavity applications and these studies were motivated by the high critical temperature (T_c) and quality factor (Q_0) of this superconductor at a given temperature, compared to Nb [2–4]; Q_0 is defined by the surface resistance (R_s) and the geometric factor (G) of a cavity as G/R_s. Nb_3Sn has lower surface resistance and a higher T_c than the Nb [5, 6]. Hence, a Nb_3Sn SRF cavity is a promising candidate to replace the current Nb SRF cavities for accelerator applications. Recently, studies at Cornell [7, 8] reported a high Q-factor of approximately 10^{10} at 4.2 K, with a maximum accelerating electric field gradient up to 17 MV m^{-1} for ~2 μm thick Nb_3Sn coatings on Nb, prepared by a vapor diffusion process. Active research in vapor diffusion Nb_3Sn films is now on-going at Fermilab, Cornell University and Jefferson Laboratory [9].

Nb_3Sn-coated cavities have been seen to quench superconductivity in the 14–17 MV m^{-1} range and some cavities still display a Q-slope, the increase of surface resistance as a function of accelerating field, figure 1(a). The surface magnetic field at which the quench occurs, ~70 mT, is, however, significantly lower than the superheating field of Nb_3Sn at ~400 mT, the ultimate limit predicted by the theory for an RF superconductor with an ideal surface [10–12]. These limits have been suggested to be a consequence of imperfections in the Nb_3Sn coatings [13], including surface roughness, thin regions, Sn-deficient regions, grain boundaries, and surface chemistry.

Recent microstructural analyses have focused on two imperfections of Nb_3Sn coatings on Nb, which are anticipated to have significant detrimental effects on the performance of Nb_3Sn coated cavities: patchy regions with extremely thin grains [14, 16, 17] and Sn-deficient regions [14, 18]. In a joint study between Fermilab and Cornell, coupons were cut out from a cavity, which exhibited a substantially degraded Q_0, see Q versus E curve for cavity ERL 1-5 displayed in figure 1(a), which was linked to localized areas with high surface resistance values. Electron microscopy was performed on coupons cut from the wall of the cavity, which revealed that areas with a high surface resistance contained grains with an abnormally large transverse length and a thickness of only ~100 nm (compared to a normal value of ~2 μm) [9, 14, 15]. The penetration depth of magnetic fields in Nb_3Sn is ~111 nm [12] and Nb_3Sn coatings require a thickness of at least ~500 nm to shield the magnetic field effectively and avoid excessive dissipation from poorly superconducting Nb/Sn compounds in the Nb_3Sn/Nb interface [14]. The formation of thin grains (<~500 nm) in the Nb_3Sn coating has been reported to be affected by a number of factors including the supply of Sn [19], pre-anodization of the Nb substrate [15], and crystallographic orientation of Nb [16]. There is some evidence that the texture and nucleation of Nb_3Sn grains could play a role but the detailed mechanism and origin of the formation of thin grains are still not understood [16]. Also, Sn-deficient regions are one of the primary concerns for Nb_3Sn SRF cavities [18]. The proportion of Sn in $Nb_{3+x}Sn_{1-x}$ ranges from ~17 to 26 at% and the T_c of Nb_3Sn varies from 6 K at ~17 at% Sn to 18.3 K at ~26 at% [1, 20]. Therefore, Sn-deficient regions with 17–19 at% Sn can decrease the T_c of Nb_3Sn coatings to below that of Nb, 9 K. The formation of Sn-deficient regions is particularly undesirable near the top surface of Nb_3Sn cavities where radiofrequency currents flow. The growth mechanism and compositional variation of Nb_3Sn have been rigorously investigated in Nb_3Sn samples prepared for superconducting wire applications by a solid-diffusion process using Cu–Sn and Nb diffusion couples, the bronze process [1, 21–25]. The compositional variation in Nb_3Sn prepared by solid-diffusion was investigated utilizing a composition gradient between a Sn-rich phase (Nb_6Sn_5) and bulk Nb, originating from the diffusion process [21, 25–27]. Low levels of Sn in Nb_3Sn have been attributed to the small formation energy of Nb antisite point defects, Nb sitting on Sn sites [26]. There is, however, little information about how Sn-deficient regions are formed during vapor diffusion preparation of a Nb_3Sn coating on Nb or about the critical role(s) played by the Nb_3Sn/Nb interface in Nb_3Sn grain growth and the formation of thin grains. The objective of the current studies is to investigate the origin of the formation of thin grains and Sn-deficient regions in Nb_3Sn coatings on Nb prepared by the vapor-diffusion process and the role of Nb_3Sn/Nb interfaces on the formation of imperfections in general.

Herein, we report on atomic-scale analyses of Nb_3Sn coatings on Nb using transmission electron microscopy (TEM), electron backscatter diffraction (EBSD) and first-principle calculations. In particular, we find that orientation relationships (ORs) at the Nb_3Sn/Nb interface are correlated with the formation of thin grains and Sn-deficient regions. Through the use of electron diffraction and high-resolution scanning transmission electron microscopy (HR-STEM), we identify four types of ORs for Nb_3Sn/Nb heterophase interfaces. Notably, large thin Nb_3Sn grains are highly correlated with a certain grain orientation relationship, specifically Nb_3Sn $(1\bar{2}0)$//Nb $(\bar{1}11)$ and Nb_3Sn (002)//Nb $(0\bar{1}1)$. Also, first-principles calculations of Nb_3Sn/Nb interfaces demonstrate that the formation of Sn-deficient Nb_3Sn close to Nb substrates is attributed to the smaller interfacial free energy of Sn-deficient Nb_3Sn/Nb interfaces compared to stoichiometric Nb_3Sn/Nb. Our findings provide evidence for understanding the

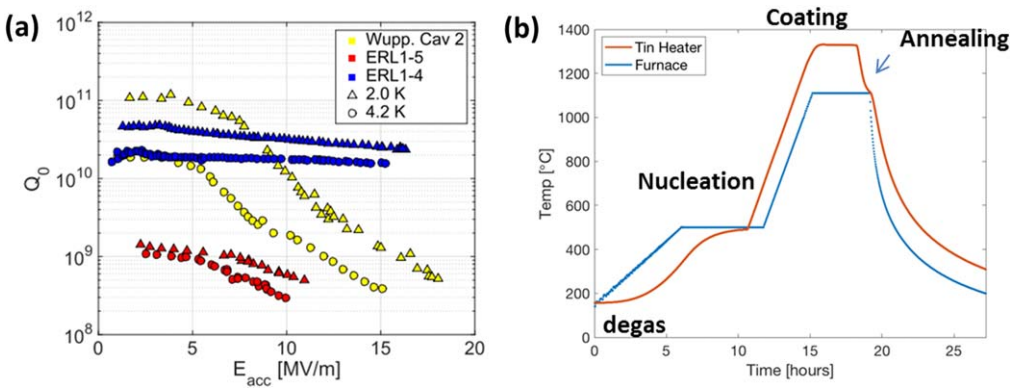

Figure 1. (a) Quality factor (Q_o) versus electric field (E) curves for different ~2 μm thick Nb_3Sn coated superconducting radiofrequency (SRF) cavities (reproduced from [14]. © IOP Publishing Ltd. CC BY 3.0). Nb_3Sn coated SRF cavity of ERL 1-4 displays a high Q_o-factor up to 15–17 MV m^{-1}, which is close to the state-of-the-art performance for a Nb_3Sn SRF cavity. ERL 1-5 exhibits a low Q_o-factor, that is, a high surface resistance. Thin-grain regions were widely observed in the Nb_3Sn SRF cavity of ERL 1-5, with a strong correlation observed between the surface resistance of Nb_3Sn and microstructures. (b) Temperature profile of substrate and tin source during the coating procedure [9, 15].

formation of imperfections in Nb_3Sn coatings on Nb, which may be used to improve the performance of Nb_3Sn SRF cavities.

2. Methodologies

2.1. Experimental procedures

Nb_3Sn coatings were prepared at the Fermi National Accelerator Laboratory and Cornell University by a vapor diffusion process, figure 1(b); for development of the process see [2, 3, 9, 10, 28, 29]. Niobium samples, tin source, and a $SnCl_2$ nucleating agent are placed in a vacuum furnace and heated to 500 °C to create nucleation sites of Nb_3Sn on the Nb surface. The furnace temperature was then raised to 1100 °C for 3.5 h to permit a Nb_3Sn coating to form on the Nb surface. The tin source was maintained at 1200 °C, so that sufficient Sn could continue to be provided to the top surface of Nb_3Sn, which subsequently diffuses into the Nb sample.

In our studies of nucleation of Nb_3Sn, only a $SnCl_2$ nucleating agent was placed in the furnace, without Sn, and then heated to 500 °C to induce nucleation. Next, the temperature was increased to 1100 °C and then cooled immediately after reaching 1100 °C.

The samples were systematically characterized by scanning electron microscopy (SEM), TEM and EBSD. A 600i Nanolab Helios focused ion-beam (FIB) microscope was employed to prepare cross-sectional samples for TEM. The samples were thinned employing a 30 kV Ga^+ ion-beam at 27 pA, and fine-polished using 5 kV Ga^+ ions at 47 pA. A Hitachi HD-8100 was used for the bright-field (BF) TEM imaging and electron diffraction analyses, and a Hitachi HD-2300 was used for STEM and energy-dispersive spectroscopy (EDS). HR-TEM images were recorded using a JEOL Grand ARM-300 and HR-STEM images were acquired using a JEOL aberration-corrected Grand ARM-200. The Gatan Micrograph Suite version 2.11 was used to analyze and process the images. EBSD data was collected using a FEI Quanta field-emission gun SEM equipped with an HKL Nordlys S camera utilizing Oxford AZtec EBSD software. The surfaces of samples were placed at a 10 mm working distance and a 30 kV electron beam with an incident angle of 20° was used for accumulating EBSD patterns. For transmission (t-) EBSD, an EM-Tec TE3 t-EBSD holder was utilized to place the surface of a TEM sample at an incident beam angle of 20°.

2.2. Computational details

The first-principles calculations in this research employed the plane-wave pseudopotential total energy method as implemented in the Vienna *ab initio* simulation package [30]. We used projector augmented wave potentials [31] and the generalized gradient approximation, developed by Perdew–Burke–Ernzerhof [32] for exchange-correlation. Unless otherwise specified, all structures are fully relaxed with respect to volume, as well as all cell-internal atomic coordinates. We considered carefully the convergence of results with respect to energy cutoff and k-points. A plane-wave basis set was used with an energy cutoff of 600 eV to represent the Kohn–Sham wave functions. A summation over the Brillouin zone for the bulk structures was performed on a 12 × 12 × 12 Monkhorst–Pack k-point mesh for all calculations and a magnetic spin-polarized method was applied for all calculations. The calculated lattice parameters of Nb and Nb_3Sn are 3.324 and 5.332 Å, respectively, which are in excellent agreement with the experimental results, 3.300 Å for Nb [33] and 5.289 Å for Nb_3Sn [34]. Both 2 × 2 × 2 and 3 × 3 × 3 supercells were used to determine the vacancy formation energies, antisite energies, and lattice substitutional energy calculations.

3. Experimental results

3.1. TEM analysis of nucleated Nb_3Sn grains

As a first step, we characterized nucleated Nb_3Sn grains in the early stages of the Nb_3Sn coating process to observe the details of the initial grain growth. The SEM micrograph in figure 2 shows nucleated Nb_3Sn grains on a Nb surface, with

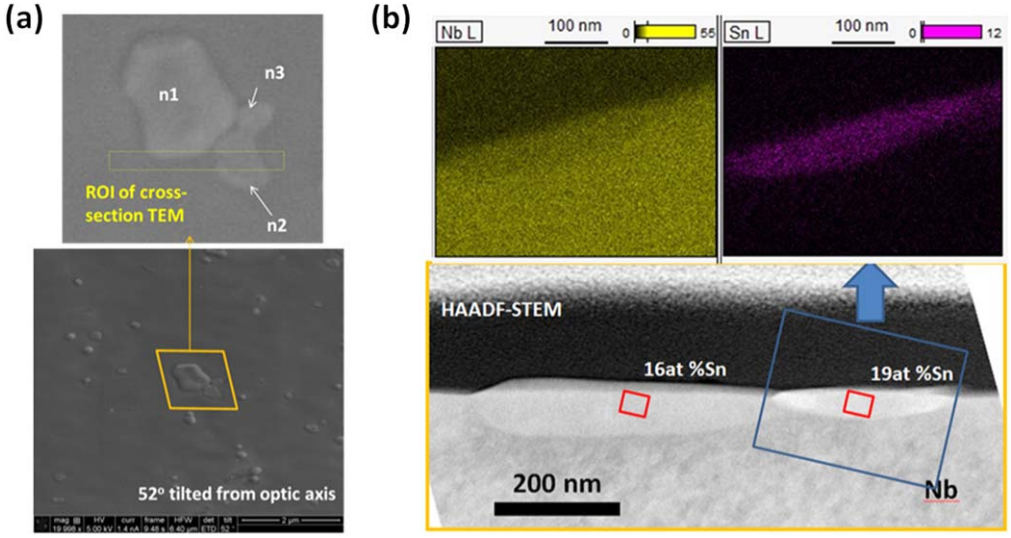

Figure 2. (a) Scanning electron microscope (SEM) images of nucleated Nb_3Sn grains prepared at Fermilab. Three nucleated grains are labeled $n1$, $n2$, and $n3$. The region for cross-sectional transmission electron microscopy (TEM) is indicated by a parallelogram. (b) High-angle annular dark-field scanning transmission electron microscope (HAADF-STEM) image and energy-dispersive spectroscopy (EDS) maps of Nb Lα (2.17 keV) and Sn Lα (3.44 keV) of the nucleated Nb_3Sn grains.

Table 1. Summary of the three regions of the Nb_3Sn coatings with different microstructures, which depend on the net Sn flux or growth rate.

	Net Sn flux (atoms nm^{-2} min^{-1})	Average growth rate (nm min^{-1})	Average thickness (μm)
Abnormally large-grain regions	322	24	~5
Normal-grain regions	161	12	~2.5
Patchy regions with thin grains	47	3.5	~0.7

some displaying lateral growth with a flat morphology. Figure 2 displays three connected nucleated Nb_3Sn grains with diameters of ~500 nm ($n1$), ~200 nm ($n2$), and ~100 nm ($n3$), respectively. Two of these nucleated Nb_3Sn grains were selected and cross-sectional TEM samples were prepared from them using a dual-beam FIB microscope. High-angle annular dark-field (HAADF) STEM images in figure 2 reveal that the thickness of the nucleated grain $n1$, was ~100 nm and that of $n2$ was ~60 nm. EDS mapping of Nb Lα (2.17 keV) and Sn Lα (3.44 keV) lines performed in the STEM mode indicates that the concentration of Sn in the nucleated Nb_3Sn grain is 16–19 at%, which is Sn-deficient compared to the nominal concentration of 25 at% Sn in Nb_3Sn.

3.2. TEM analyses of Nb_3Sn grains

The microstructures of the Nb_3Sn coating and the Nb_3Sn/Nb interfaces were analyzed employing BF-TEM, HAADF-STEM, EDS, and HR-S/TEM after the coating process was completed. The results displayed significant variations in the microstructures with respect to the net Sn flux, which was estimated by taking the average thickness of the Nb_3Sn coating and the coating process time. It is possible to distinguish three different regions (table 1): (1) abnormally large-grain regions for a high Sn flux; (2) normal grain size regions for a medium Sn flux; and (3) patchy regions with thin grains for a low Sn flux.

3.2.1. Abnormally large Nb_3Sn grain regions (average growth rate: 24 nm min^{-1}). In the case of a high net Sn flux (high average growth rate of 24 nm min^{-1}), we observed regions with abnormally large and irregularly shaped Nb_3Sn grains, SEM image of figure 3(a), recorded using a secondary-electron (SE) detector. The regions have a rounded-shape and a size that varies from tens to hundreds of microns. Abnormally large grain size regions have bright contrast, compared to neighboring regions with normal-size grains, possibly due to topological effects from the rough Nb_3Sn surface. HAADF-STEM imaging of a cross-section of Nb_3Sn/Nb, figure 3(c), yields both the grain size and thickness, ~5 μm for each. STEM-EDS analyses of the abnormally large grains reveal a concentration of ~26 at% Sn, which is similar to normal Nb_3Sn grains, suggesting that the stoichiometry of the abnormally large grain regions is also Nb_3Sn. The round shape of the abnormally large grain regions and the irregular outline of large Nb_3Sn grains in the region imply the abrupt formation of Nb_3Sn phases from a liquid droplet of Sn, which is discussed further in section 4.1.

3.2.2. Normal Nb_3Sn grain regions (average growth rate: 12 nm min^{-1}). The HAADF-STEM image in figure 4(c) demonstrates that the Nb_3Sn coatings on Nb are approximately 2.5 $\pm$ 1.0 μm thick, with its surface features revealed in the SE-SEM image, figure 4(a). The sample in the SEM image was tilted by 52° from the SEM's optic axis to display the granular

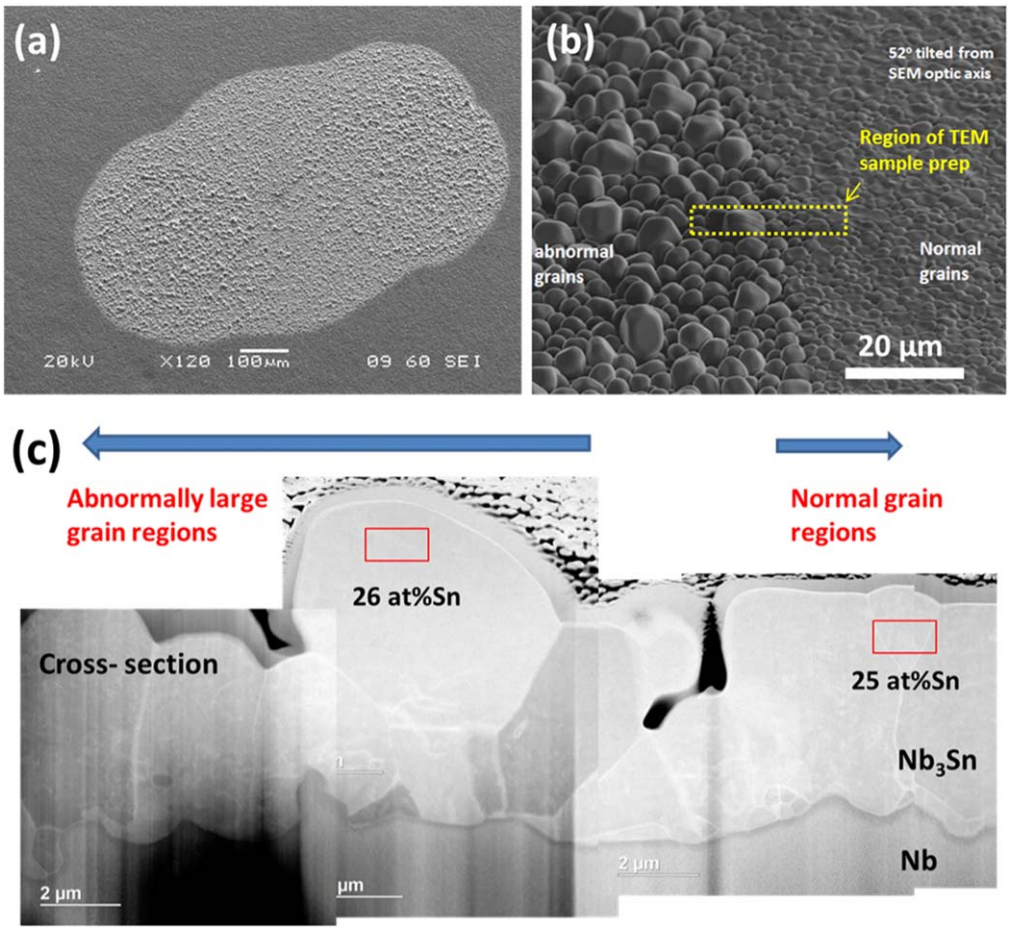

Figure 3. (a) SEM image of abnormally large grain regions of the Nb_3Sn coating prepared at Fermilab, (b) SEM image of the boundary between abnormally large-grain regions and normal grain regions tilted by 52° from the SEM's optic axis. (c) HAADF-STEM image of a cross-section of Nb_3Sn/Nb across regions with normal grains and abnormally large grains. The composition of one of the abnormally large grains is estimated using STEM-EDS analyses exhibiting similar values (26 at% Sn compared to 25 at% Sn in the normal grains).

roughness of the surface. Utilizing SEM imaging, the average grain size for two samples, A5 and A10, is $2.0 \pm 0.6\,\mu$m. Quantitative analyses of the Nb_3Sn coatings employing STEM-EDS reveals the presence of Sn-deficient regions. Most of these regions are close to the Nb substrate, although they are occasionally observed in the middle of Nb_3Sn grains, figure 4(d). Quantification of the composition of two Sn-deficient regions (numbers 1 and 3) is ≈19 at% Sn compared to the anticipated value of 25 at% Sn for stoichiometric Nb_3Sn.

Next, we analyzed the Nb_3Sn/Nb interfaces utilizing BF-TEM, HR-TEM and electron diffraction. The results yield ORs between Nb_3Sn and Nb at the Nb_3Sn/Nb interface. Figure 5(a) displays a HR-TEM image of the Nb_3Sn/Nb interface in normal Nb_3Sn grain regions. The HR-TEM image was recorded for a Nb $[\bar{1}11]$ zone axis, which reveals the ORs of the Nb_3Sn grains with the Nb substrate. One grain (labeled Orientation A) has an OR with Nb of Nb_3Sn $(1\bar{2}0)//Nb$ $(\bar{1}11)$ and Nb_3Sn $(002)//Nb$ $(1\bar{1}2)$, while another grain (labeled Orientation C) is Nb_3Sn $(1\bar{2}0)//Nb$ $(\bar{1}11)$ and Nb_3Sn $(002)//Nb$ $(0\bar{1}1)$. Owing to the OR of two grains at a Nb_3Sn/Nb interface a $[1\bar{2}0]$ tilt grain boundary with 29° tilt-angle is formed. The HAADF-STEM image in figure 5(b) exhibits another OR at the Nb_3Sn/Nb interface for a Nb [011] zone axis. As seen in figure 5(c), the electron diffraction pattern of one of the grains at the Nb_3Sn/Nb interface (indicated by the red-dotted circle in figure 5(b)) has the following ORs: Nb_3Sn $(002)//Nb$ (011) and Nb_3Sn $(130)//Nb$ (002) (termed Orientation D).

3.2.3. Patchy regions with thin Nb_3Sn grains (average growth rate: 5 nm min^{-1}). As previously reported [9, 14, 35], patchy regions including thin grains with a large lateral grain size of up to many tens of microns form in regions with a low net Sn flux of ∼47 Sn atoms nm^{-2} min (slow average growth rate of ∼5 nm min^{-1}). The HAADF-STEM image in figure 6 presents one of the patchy regions with thin Nb_3Sn grains (grains numbers 1 and 5). The ORs of the Nb_3Sn/Nb interface, of the seven grains in the TEM sample, were analyzed by electron diffraction or HR-TEM, which are displayed in figure 6. The first grain to be analyzed is the relatively thick grain (grain number 3). Compositional variations within the regions of grains numbers 3 and 4 are examined by STEM-EDS, figure 7(c), which reveals that there are low levels of Sn in portions of the Nb_3Sn/Nb interface [18]. Atomically-resolved HR-STEM images of the Nb_3Sn/Nb interface for grain number 3 were recorded using a JEOL

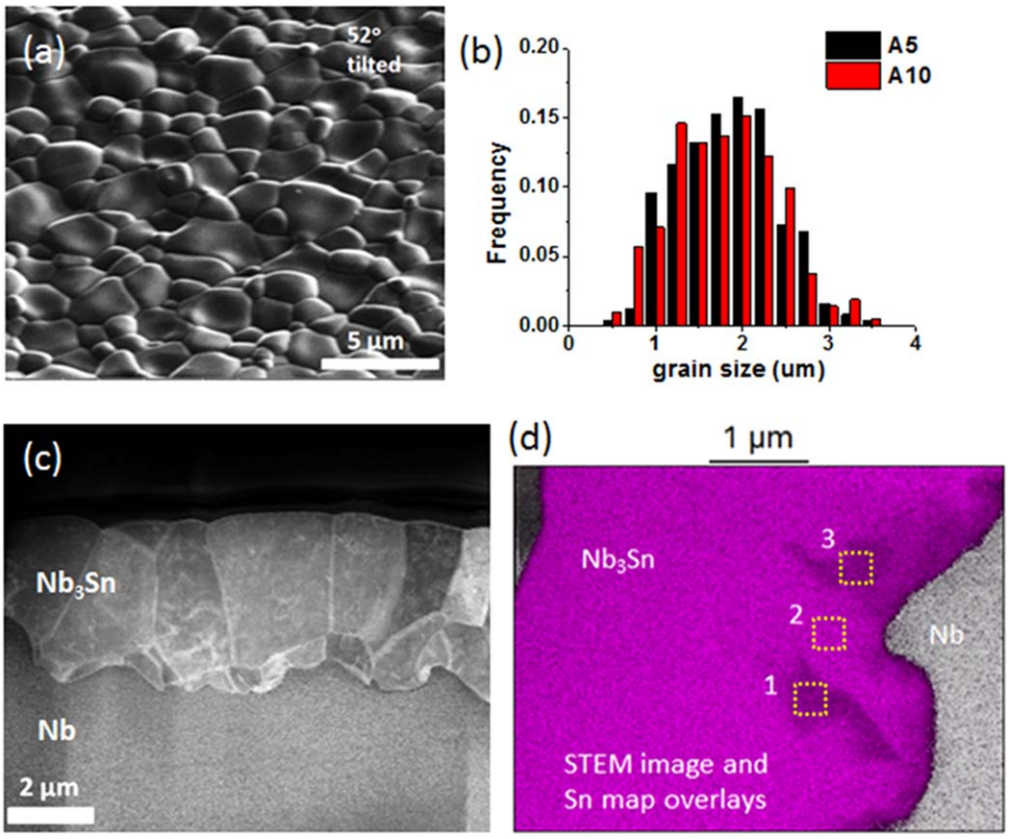

Figure 4. (a) SEM image of a Nb_3Sn surface, which displays roughness due to the granularity of Nb_3Sn (the surface was tilted 52° from the SEM's optic axis). The samples were coated at Fermilab. (b) Histogram of grain sizes (diameters) of A5 and A10 samples with an average grain size of 2.0 ± 0.6 μm. (c) A cross-sectional view of a Nb_3Sn film on Nb, obtained using HAADF-STEM. (d) An HAADF-STEM image and overlays of the STEM image and EDS Sn L map on it. Sn-deficient regions are observed near bulk Nb (denoted by 1 and 3). The tin concentration of region numbers 1 and 3 is 19 at%, while that of region number 2 is 25 at%.

aberration-corrected Grand ARM-200, figure 7(a). This interface displays epitaxial growth of Nb_3Sn on Nb with Orientation A, Nb_3Sn $(1\bar{2}0)//Nb$ $(\bar{1}11)$ and Nb_3Sn $(002)//Nb$ $(1\bar{1}2)$ agreeing with the electron diffraction pattern of this interface in figure 7(b). The interplanar distance of Nb_3Sn (002) is 2.63 Å (JCPDS No. 04-017-6755), while the value for Nb $(1\bar{1}2)$ is 2.70 Å (JCPDS No. 00-035-0789), which results in an ~2.8% lattice mismatch and produces a tensile strain in the Nb_3Sn grain along the [002] direction. There are additional misfit dislocations at the Nb_3Sn/Nb interface due to the lattice mismatch between Nb_3Sn and Nb. Another OR, Orientation B, is observed in grains numbers 2 and 4. As observed in the electron diffraction pattern of the Nb_3Sn/Nb interface of grain numbers 2 and 3, figure 8(a), the (002) plane of Nb_3Sn grain number 2 is parallel to Nb $(23\bar{1})$, which implies that grain number 2 is tilted by 8.9° about the Nb_3Sn $[1\bar{2}0]$ axis from grain number 3 with Orientation A. The HR-TEM image of grain numbers 2 and 3, figure 8(b), demonstrates that the Nb_3Sn grains form an 8.9°/$[1\bar{2}0]$ tilt grain boundary.

Grain number 5 was analyzed as a representative of the thin grains. HR-STEM imaging of the Nb_3Sn/Nb interface with the thin-grain number 5 is displayed in figure 9(a) and it possess Orientation C, Nb_3Sn $(1\bar{2}0)//Nb$ $(\bar{1}11)$ and Nb_3Sn $(002)//Nb$ $(0\bar{1}1)$. For Orientation C, the Nb_3Sn/Nb interface has a large lattice mismatch (12.3%) between the Nb_3Sn (002) plane with $d = 2.63$ Å and the Nb $(0\bar{1}1)$ plane with $d = 2.34$ Å. Indeed, a high density of misfit dislocations, representing extra Nb $(0\bar{1}1)$ planes, is observed in the HR-STEM image, figure 9. The misfit dislocations appear at approximately every eight Nb $(0\bar{1}1)$ planes at the interface, which is in agreement with the lattice mismatch of 12.3%. A STEM-EDS map of the thin-grain in figure 9(b) reveals that an ~100 nm thick Sn-deficient layer exists at the Nb_3Sn/Nb interface, probably due to the high compressive strain on the Nb_3Sn $(1\bar{2}0)$ plane. The increase of the lattice parameter of Nb_3Sn by adding Sn $(\frac{1}{a}\frac{da}{dc})$ is $\approx 2.6 \times 10^{-4}$ per at% of Sn [36], which leads to a volume size factor (Ω_{sf}) of Sn in Nb_3Sn of 8% [37]. An HR-TEM study of another thin-grain (grain number 1) displays the same OR as the thin Nb_3Sn grain (grain number 5): see supplementary figure S.1 available online at stacks.iop.org/SUST/32/024001/mmedia. Orientations A, B, C, and D and their lattice mismatches are summarized in table S.1. The lattice mismatches are estimated assuming stoichiometric 25 at% Sn Nb_3Sn since the difference of the lattice parameter of Nb_3Sn between 17 and 25 at% Sn is small, ~0.2% [36].

Transmission (t-) EBSD was performed to identify the misorientation axes and angles of Orientations A, B and C, figure 6. For Orientation A and B, both have an ~40° rotation

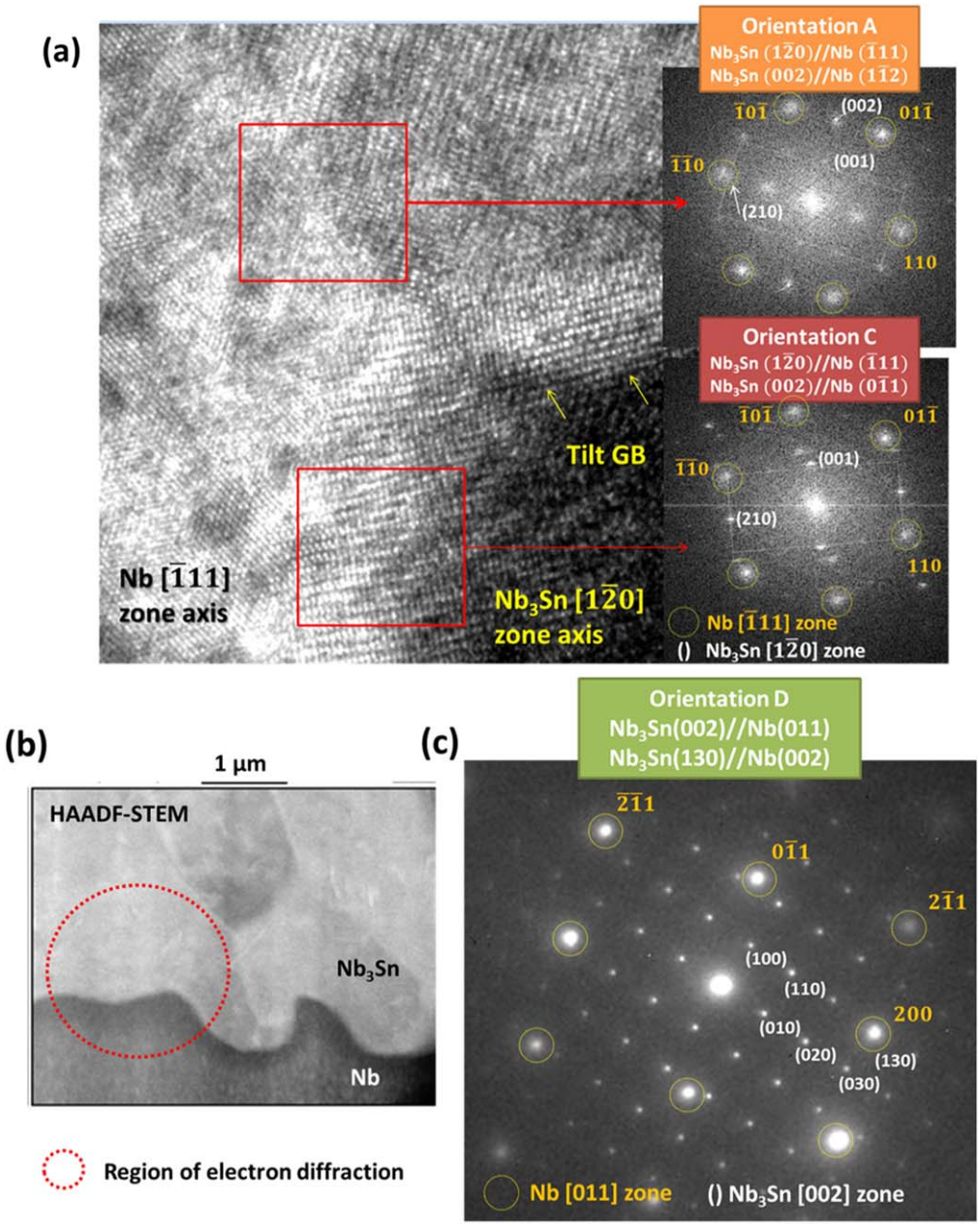

Figure 5. (a) HR-TEM image of Nb_3Sn/Nb for normal grain regions, showing two grains grown epitaxially on Nb with their orientation relationships. The Nb_3Sn coating was prepared at Cornell University. The orientation relationships correspond to a 29°/[1$\bar{2}$0] tilt grain boundary. (b) HAADF-STEM image of a Nb_3Sn/Nb interface with a Nb [011] zone axis. The region for the electron diffraction pattern is indicated by a red-dotted circle. The sample was prepared at Fermilab. (c) The electron diffraction pattern of the Nb_3Sn/Nb interface yields the following orientation relationships, Nb_3Sn (002)//Nb (011) and Nb_3Sn (130)//Nb (002), termed Orientation D.

angle about the ⟨334⟩ rotation axis between Nb_3Sn and Nb. They are not clearly distinguishable due to the small misorientation angle between Orientations A and B, 8.9° about the ⟨120⟩ axis, and deviations of the Euler angle measurements (~3°) determined from the EBSD patterns. Orientation C displays ⟨123⟩ or ⟨124⟩ rotation axes with ~50° of rotation, see table S.2. The misorientation axes and rotation angles of Orientations A, B and C were used to analyze the ORs of normal grain regions and patchy regions with thin grains comparatively, using normal or transmission EBSD, section 4.2.

3.3. Vacancy formation and antisite substitutional behavior in Nb_3Sn

We used first-principles calculations to understand the formation of Nb and Sn antisite defects and vacancies. The vacancy formation energies, E_v, for both Nb and Nb_3Sn are described using a 2 × 2 × 2 supercell employing the following equation [38]:

$$E_v = E_v^{tot} - E_{bulk}^{tot} + \mu, \quad (1)$$

where E_v^{tot} is the total energy of the supercell with a vacancy,

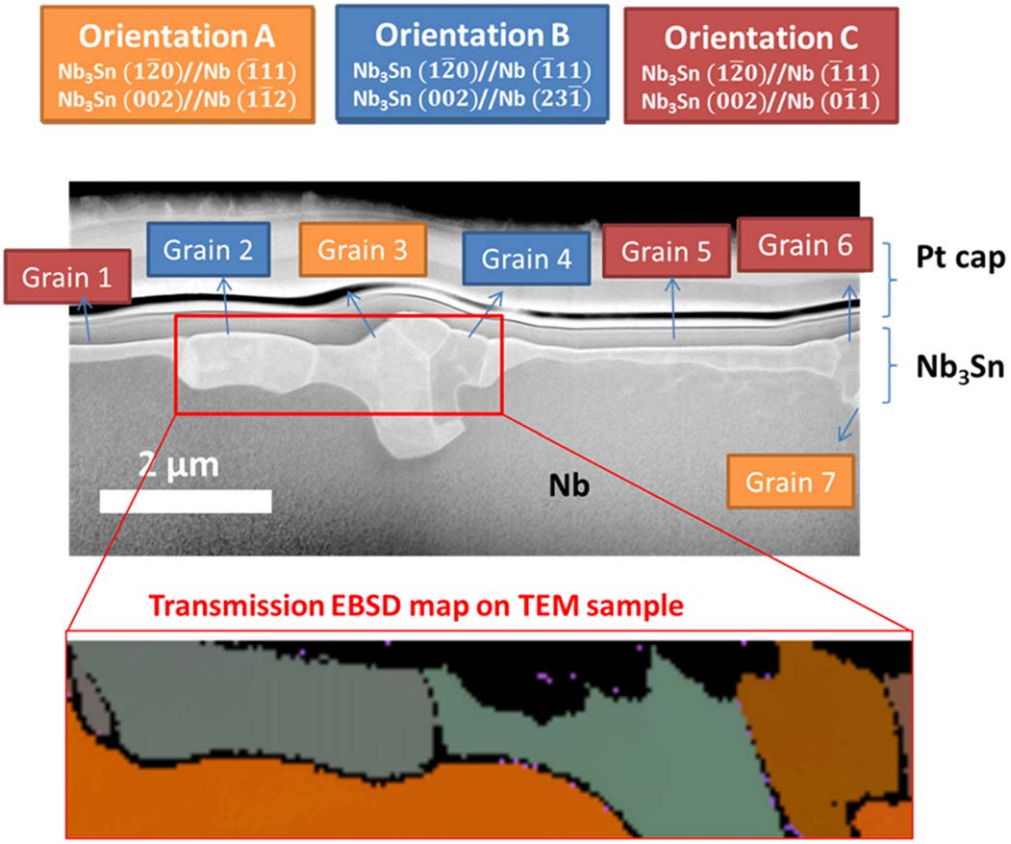

Figure 6. HAADF-STEM image of the patchy region with thin Nb_3Sn grains. Three types of orientation relationships (Orientations A, B, and C) are observed. Transmission EBSD mapping of four grains, grains numbers 2–5, was conducted to identify the misorientation axes and angles for Orientations A, B, and C. The Nb_3Sn film was coated at Fermilab.

E^{tot}_{bulk} is the total energy of the supercell without a vacancy, and μ is the chemical potential of the atom removed from the vacancy site. Our calculations yield the following results: (i) E_v is 2.82 eV/atom for Nb in bulk Nb; (ii) 3.95 eV/atom for Sn in Nb_3Sn; and (iii) 2.04 eV/atom for Nb in Nb_3Sn. A Nb vacancy in Nb_3Sn has a smaller formation energy and thus is more readily formed than a Sn vacancy in Nb_3Sn. Both Nb and Sn vacancies play a major role for understanding bulk diffusion in Nb_3Sn.

The antisite substitutional structures were modeled by allowing either Nb or Sn to substitute at either the Sn or Nb sublattice sites in both the $2 \times 2 \times 2$ and $3 \times 3 \times 3$ Nb_3Sn superlattices and then fully relaxing the structures. The antisite energies in Nb_3Sn were calculated employing the following equations [38, 39]:

$$E_{\mathrm{Nb}\rightarrow\mathrm{Sn}} = (E^{tot}_{\mathrm{Nb_3(Sn_{1-x}Nb_x)}} + \mu_{\mathrm{Sn}}) - (E^{tot}_{\mathrm{Nb_3Sn}} + \mu_{\mathrm{Nb}}), \quad (2)$$

$$E_{\mathrm{Sn}\rightarrow\mathrm{Nb}} = (E^{tot}_{\mathrm{(Nb_{1-y}Sn_y)_3Sn}} + \mu_{\mathrm{Nb}}) - (E^{tot}_{\mathrm{Nb_3Sn}} + \mu_{\mathrm{Sn}}), \quad (3)$$

where μ_i is the chemical potential of Nb or Sn, $E^{tot}_{\mathrm{Nb_3Sn}}$ is the total energy of Nb_3Sn, $E^{tot}_{\mathrm{Nb_3(Sn_{1-x}Nb_x)}}$ is the total energy of Nb_3Sn with Nb at a Sn sublattice site, and $E^{tot}_{\mathrm{(Nb_{1-y}Sn_y)_3Sn}}$ is the total energy of Nb_3Sn with Sn in a Nb sublattice site. The first-principles results in table 2 demonstrate that a Nb antisite atom forms more readily than a Sn antisite atom in both the $2 \times 2 \times 2$ and $3 \times 3 \times 3$ Nb_3Sn superlattices, because $E_{\mathrm{Nb}\rightarrow\mathrm{Sn}}$ is significantly smaller than $E_{\mathrm{Sn}\rightarrow\mathrm{Nb}}$. The Nb antisite atom generates both smaller average atomic forces and local atomic displacements. The experimental results in this study demonstrate the presence of Sn-deficient regions close to the Nb substrate and the first-principle calculations indicate that Sn-deficient Nb_3Sn is a Nb antisite compound, with Sn sites being replaced by Nb atoms, with Nb vacancies as secondary point defects with small concentrations of Sn vacancies due to their high vacancy formation energy.

4. Discussion

4.1. Effect of Sn flux (growth rate) on the microstructure of Nb_3Sn on Nb

This study describes the microstructure of three regions of the Nb_3Sn coatings on Nb, which are formed by different rates of a net Sn flux (or average growth rate). As table 1 demonstrates, the microstructure of a Nb_3Sn coating is affected strongly by the net Sn flux during its formation. This is important because a homogeneous high-quality Nb_3Sn coating on Nb with a reasonably smooth surface, no uncoated regions or thin grains, and smaller composition variations is critical for the performance of Nb_3Sn SRF cavities to avoid heating at microstructural imperfections. A uniform Nb_3Sn coating with an average grain size of 2 ± 0.6 μm and a thickness of $\sim$2.5 μm was obtained with a medium Sn flux

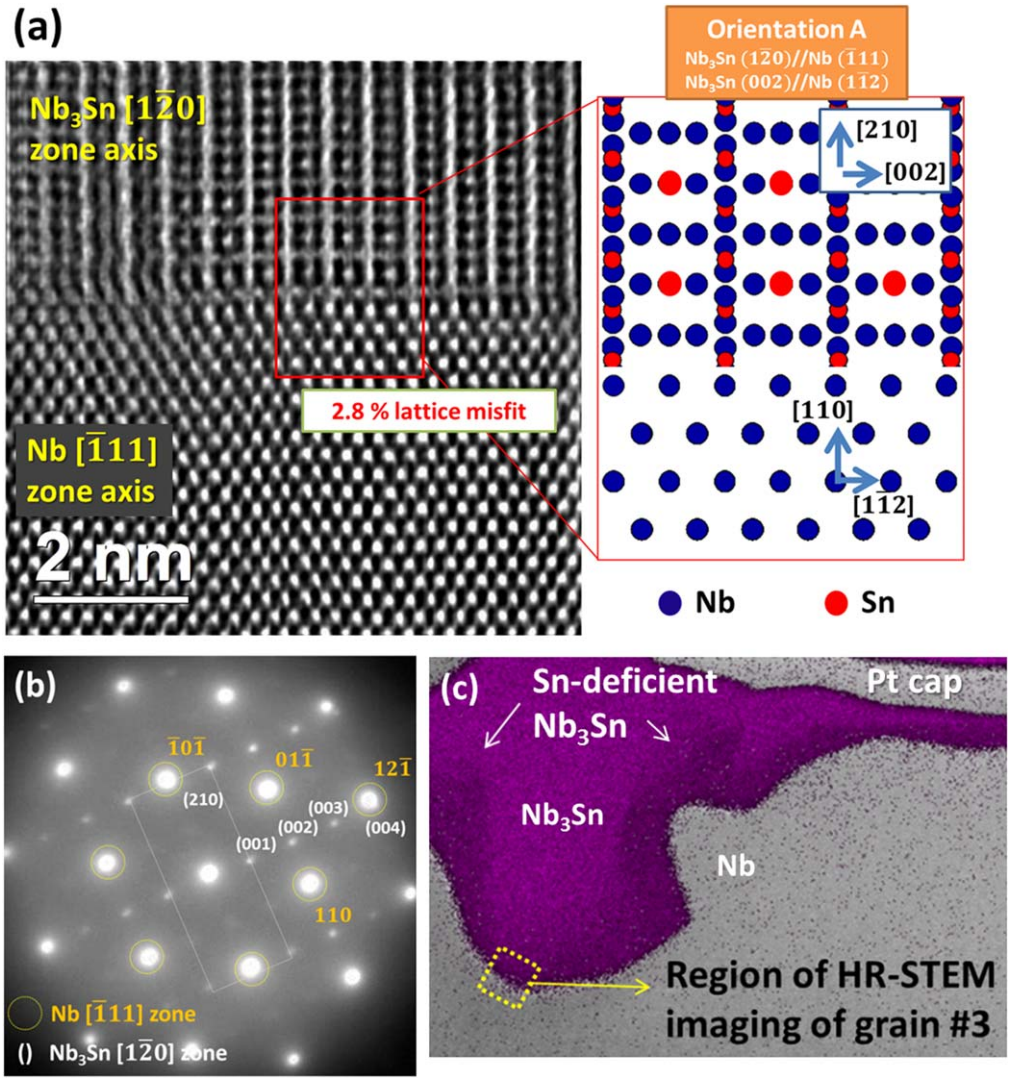

Figure 7. (a) Atomically-resolved HR-STEM image of the Nb_3Sn/Nb interfaces of grain number 3 and corresponding atomic configurations displaying epitaxial growth of Nb_3Sn on Nb with Orientation A, right-hand side. The solid-red circles are Sn atoms and the solid-blue circles are Nb atoms. (b) Corresponding electron diffraction pattern of the Nb_3Sn/Nb interface of grain number 3. (c) Overlays of STEM-EDS Sn Lα (3.44 keV) mapping of the region of grain numbers 3, 4 and 5 and HAADF-STEM image display compositional variations in the Nb_3Sn grains. The area of the HR-STEM image is denoted by a yellow dotted square.

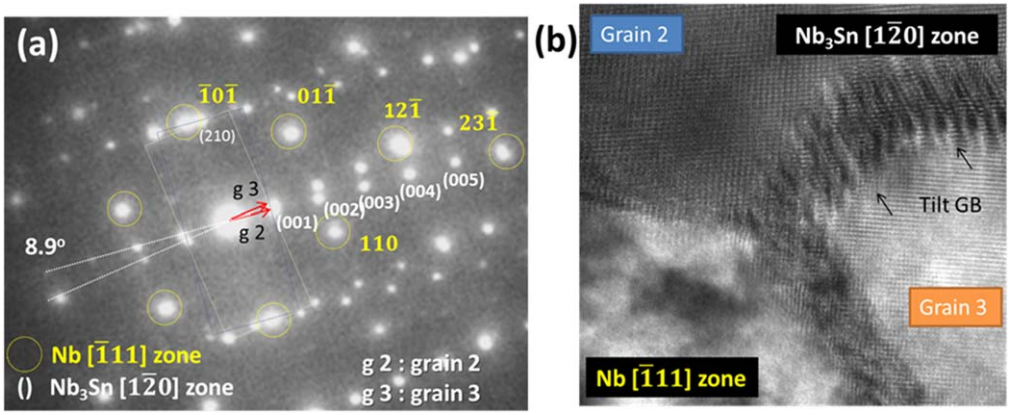

Figure 8. (a) Electron diffraction pattern of the Nb_3Sn/Nb heterophase interface of grain numbers 2 and 3. The (002) plane of Nb_3Sn grain number 2 is parallel to the (23$\bar{1}$) plane of Nb, denoted Orientation B. (b) HR-TEM image of the Nb_3Sn/Nb interface of grain numbers 2 and 3, showing the formation of an 8.9°/[1$\bar{2}$0] tilt GB.

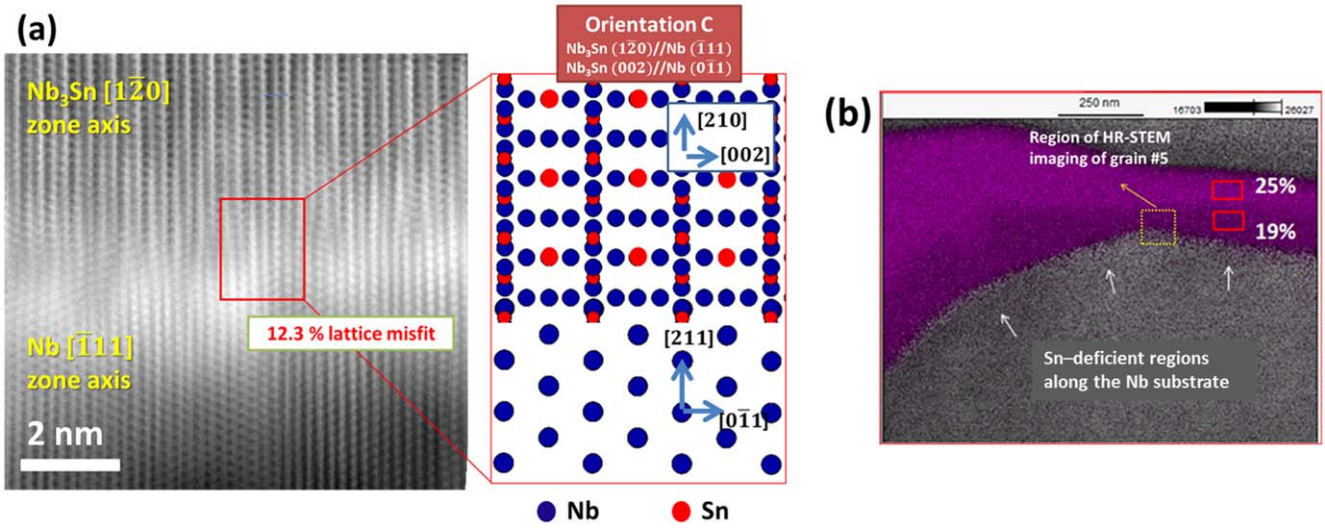

Figure 9. (a) Atomically-resolved HR-STEM image of the Nb_3Sn/Nb heterophase interface of grain number 5 with Orientation C, and corresponding atomic configurations showing epitaxial growth of Nb_3Sn on Nb, right-hand side. The solid-red circles are Sn atoms and the solid-blue circles are Nb atoms. (b) HAADF-STEM-EDS Sn L map of grain number 5. The region of the HR-STEM image at the Nb_3Sn (grain number 5)/Nb heterophase interface is indicated by a yellow dotted square.

whose value is about 161 Sn atoms nm^{-2} min, figure 4 and table 1. Our results indicate that the Sn flux has a strong influence on the kinetics of Nb_3Sn's nucleation and growth during the coating process. A large net Sn flux (322 Sn atoms nm^{-2} min), and a growth rate of 24 nm min^{-1} are associated with the formation of abnormally large grains (more than 5 μm) and a rough surface topology of a Nb_3Sn coating, figure 3. This is probably due to the abrupt formation of Nb_3Sn grains with the concomitant formation of liquid Sn droplets on the surface. The melting temperature of Sn is low, 231.9 °C, so that Sn is in the liquid state at the process temperature, 1100 °C. Therefore, if the flux of Sn atoms from the vapor phase is greater than the diffusion of Sn into bulk Nb_3Sn, Sn may accumulate on the surface and form liquid droplets on top of Nb_3Sn. This supposition is supported by the round morphology of the abnormally large grain regions representing Sn droplets formed in a range of diameters, from tens to hundreds of microns, when using a high Sn flux, figure 3(a). In contrast, patchy regions with ~200 nm thick thin grains with a large lateral diameter more than ~4 μm, appear on the surface in the region with low net Sn flux (47 Sn atoms nm^{-2} min^{-1}). This indicates that the nucleation of Nb_3Sn is non-uniform and some of the thin grains outgrow others in a lateral direction. Details of the origin of the thin Nb_3Sn grains are discussed in section 4.3.

4.2. Orientation relationships (ORs) at Nb_3Sn/Nb

In addition to the effect of the Sn flux on the microstructure of Nb_3Sn, the primary finding is that Nb_3Sn/Nb heterophase interfaces play a critical role in the formation of imperfections in Nb_3Sn coatings, such as thin grains and Sn-deficient regions. Specifically, a strong correlation exists between the formation of thin grains and Orientation C, figure 9. Four types of ORs for the Nb_3Sn/Nb heterophase interfaces (Orientations A, B, C and D) were found and three of these ORs (Orientation A, B, C) were frequently observed on the zone axis of Nb [$\bar{1}$11] with Nb_3Sn [1$\bar{2}$0], figure 6, which suggests that these interfaces have lower interfacial free energies than alternative interfaces.

It is also noteworthy that the ORs, in particular, Orientations A, B and C, were observed more frequently in patchy regions for the case of a low Sn flux compared to medium and high Sn-fluxes. EBSD and transmission EBSD analyses were employed to analyze ORs of Nb_3Sn/Nb heterophase interfaces in normal grain regions and patchy regions with thin grains, figure 10 and table 3. A total 66 interfaces of normal grain regions and 13 interfaces of patchy regions with thin grains were analyzed and the latter display a higher frequency of Orientations A, B and C, ~ 69%, compared to the interfaces in normal grain regions, ~17%, table 3. This is probably because the small Sn flux results in slow growth of Nb_3Sn grains, providing sufficient time for the Sn atoms to diffuse into the Nb substrate and form a stable Nb_3Sn/Nb interface.

4.3. Origin of the formation of thin grains

Grains with Orientation C [Nb_3Sn (1$\bar{2}$0)//Nb ($\bar{1}$11) and Nb_3Sn (002)//Nb (0$\bar{1}$1)] are consistently significantly thinner than the other grains, indicating that the interfacial migration rate of these grains is slower than that of the other grains. The slow interfacial migration rate can be rationalized by the high dislocation density of misfit dislocations due to a large lattice mismatch, 12.3%. The HR-STEM image, figure 9, demonstrates that the misfit dislocations are separated by ~2 nm. The migration of these interfaces requires climbing and/or gliding of the misfit dislocations and the energy required for these processes could retard the velocity of the reaction front [40, 41].

Table 2. The antisite energies, average atomic force and displacement at the first nearest-neighbor distances associated with antisite substitutions, determined by first-principles calculations.

	Supercell	$E_{antisite}$ (eV atom^{-1})	Average atomic force (eV Å^{-1})	Average atomic displacement (Å)
$E_{Nb\rightarrow Sn}$	2 × 2 × 2	0.325	0.016 74	0.0311
	3 × 3 × 3	0.268	0.012 51	0.0227
$E_{Sn\rightarrow Nb}$	2 × 2 × 2	0.718	0.031 18	0.0419
	3 × 3 × 3	0.637	0.028 86	0.0344

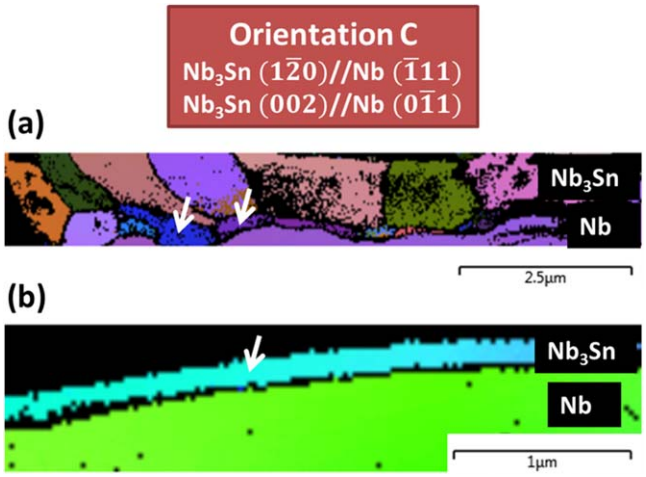

Figure 10. Transmission EBSD map of (a) normal grain regions and (b) patchy regions with thin grains. Two grains among 15 grains in the TEM sample with normal regions (a) have Orientation C, denoted by white arrows. Also, the thin-grain (b) has Orientation C. TEM sample (a) was prepared at Fermilab and sample (b) was prepared at Cornell University.

Table 3. Statistics of orientation relationships at Nb_3Sn/Nb interfaces in normal Nb_3Sn regions and patchy regions with thin Nb_3Sn grains. Sixty-six grains were analyzed in the normal regions and thirteen grains were analyzed in the patchy regions with thin thin grains using EBSD, transmission EBSD, and TEM analyses.

	Frequencies	
Orientation type	Normal Nb_3Sn regions ($N = 66$)	Patchy regions with thin Nb_3Sn grains ($N = 13$)
Orientation A	5%[a]	15%
Orientation B		15%
Orientation C	12%	39%
Others	83%	31%

[a] Orientation A and B are not distinguishable in transmission (t-) EBSD due to the deviations of the Euler angles in the EBSD data (see table S.2 in supplementary information).

The influence of ORs on the interfacial migration rate, during a solid-state reaction, has been reported for other systems, especially growth of a spinel on MgO or sapphire (Al_2O_3) [40–48]. For $MgAl_2O_4$ spinel-growth between MgO and Al_2O_3, the $MgAl_2O_4$/MgO interface is pinned by a high misfit dislocation density; one dislocation every ~23 atomic plane of (010) $MgAl_2O_4$, caused by the large lattice mismatch ($2\frac{a_{MgAl_2O_4} - 2a_{MgO}}{a_{MgAl_2O_4} + 2a_{MgO}} \approx -4.3\%$) [47]. Similarly, for $ZnAl_2O_4$ growth between ZnO and Al_2O_3, the reaction at the $ZnAl_2O_4$/ZnO interface, which has a large lattice mismatch (−13.7%), is limited due to dislocation gliding and/or climbing, while the $ZnAl_2O_4/Al_2O_3$ interface with a smaller lattice mismatch (2.1%) is relatively mobile [45]. Interfacial migration of an interface with a large lattice mismatch requires climb of the misfit dislocations at the interface, which is the rate-limiting step [45, 47]. In the case of Nb_3Sn, the nucleated grain with Orientation C may preferentially spread in the lateral direction rather than increasing its thickness. This would give rise to the formation of abnormally large thin grains during the early stage of Nb_3Sn growth. The formation of large thin grains significantly reduces the Sn supply to the Nb_3Sn/Nb interface due to the decreased density of grain boundaries (which act as short-circuit diffusion pathways). As a result, the interfacial reaction rate at Nb_3Sn/Nb becomes even slower.

Another factor that influences the formation of thin Nb_3Sn grains is the growth rate [49]. Thin grains with a large lateral diameter appeared when the average growth rate was slow (~3.5 nm min^{-1}) as a consequence of a small net Sn flux (~47 Sn atoms nm^2 min^{-1}), and they are not observed in medium and high net Sn-flux regions. The experimental evidence in this article is not sufficient to demonstrate that the average Sn flux during the coating process is represented by the net Sn flux measured after coating, but it is logical that a high average Sn flux could help prevent the growth of large thin grains. When the Sn flux is high, the density of nucleation sites increases and, therefore, the lateral growth of the thin grains is limited due to the competition with neighboring Nb_3Sn grains.

4.4. Formation of Sn-deficient regions: nucleation and their evolution

In the Nb–Sn binary phase diagram [1, 20], Nb_3Sn has a wide range of Sn composition from ~17 to 26 at% Sn and the composition of Nb_3Sn in the two-phase equilibrium phase-field (α-Nb plus Nb_3Sn) is ~17 at% Sn at 1100 °C. Therefore, it is reasonable that the nucleated Nb_3Sn grains at the Nb_3Sn/Nb heterophase interface have ~17 at% of Sn concentration, figure 2. As discussed, the Sn-deficient regions are probably initially formed at the Nb_3Sn/Nb heterophase interface and the Sn deficiency in the middle of a grain is a consequence of slow Sn diffusion, ~100 nm h^{-1} [50], in Nb_3Sn. First-principle calculations revealed that the Nb antisite defect has a small formation energy, ~0.3 eV/atom (table 2) and the formation of Sn-deficient regions may be

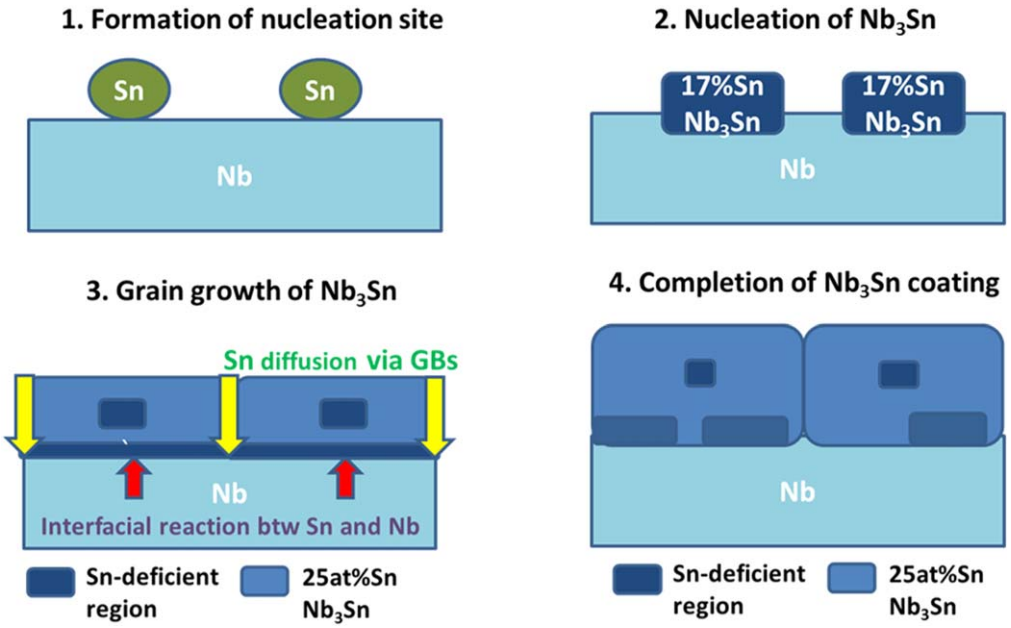

Figure 11. Schematic diagram for proposed coating process of Nb_3Sn on Nb employing vapor diffusion of Sn. The nucleated embryos of Nb_3Sn in step 2 (nucleation of Nb_3Sn) grow laterally to form a continuous layer of Nb_3Sn, which has regions that are deficient in Sn (step 3—grain growth of Nb_3Sn). In step 4 (formation of a complete layer of Nb_3Sn), note the presence of a grain boundary, which is an important short-circuit for diffusion of Sn toward the Nb_3Sn/Nb heterophase interface.

Table 4. The interfacial internal energy of four different orientations at 0 K calculated using first-principles calculations. Unit: mJ m^{-2}.

Orientation relationship	Interface type	Perfect Nb_3Sn	Sn-deficient[a] Nb_3Sn
A	Nb_3Sn $(1\bar{2}0)$//Nb $(\bar{1}11)$	262	229
A	Nb_3Sn (002)//Nb $(1\bar{1}2)$	208	186
A	Nb_3Sn (210)//Nb (110)	274	233
B	Nb_3Sn (002)//Nb $(23\bar{1})$	223	195

[a] The interfacial structure is Nb/Nb_3Sn. The Nb slab has 66 atoms and the Nb_3Sn slab has 64 atoms. Three Nb antisites are employed in the Sn-deficient Nb_3Sn slab resulting in 20.3 at% Sn.

assisted by the small formation energy of Nb antisite defects [26, 34, 50]. The concentration of Sn-deficient regions is 17 to 19 at% Sn, and this implies that 0.24–0.32 fraction of Sn sites are occupied by Nb atoms in these regions.

The interfacial energy of the Nb/Nb_3Sn heterophase interface is essential for understanding the mechanisms and stability of this heterophase interface with vicinal orientations. Specifically, the interfacial energy plays a critical role in the nucleation of Nb_3Sn because the strain energy and the formation energy of Nb antisite defects are negligible compared to the interfacial energy in the nucleation stage [51–53]. We calculate the energies of the four simple interfaces with Orientations A and B, which our experiments detected: (i) Nb_3Sn $(1\bar{2}0)$//Nb$(\bar{1}11)$; (ii) Nb_3Sn(002)//Nb$(1\bar{1}2)$; (iii) Nb_3Sn(210)//Nb(110) with Orientation A; and (iv) Nb_3Sn(002)//Nb$(23\bar{1})$ with Orientation B. Orientation C is excluded because it exhibits abnormal Nb_3Sn growth and difficult to simulate using first-principles calculations due to the large lattice mismatch. The interfacial configurations were constructed with the initial positions based on ideal Nb and Nb_3Sn phases; the latter was stretched to match the Nb phase. We subsequently fully relaxed all the atomic positions, with the unit vector normal to the (*hkl*) plane of the interface. The interfacial internal energies at 0 K are calculated by subtracting the total energy of the phases on either side of the interface from the total energy of a two-phase system containing an interface:

$$\sigma_{\mathrm{Nb/Nb_3Sn}} = \frac{1}{2A}[E^{tot}_{\mathrm{Nb/Nb_3Sn}} - (E^{tot}_{\mathrm{Nb}} + E^{tot}_{\mathrm{Nb_3Sn}})], \qquad (4)$$

where A is the interfacial area, E^{tot}_{Nb} is the total internal energy of the Nb phase, $E^{tot}_{\mathrm{Nb_3Sn}}$ is the total internal energy of the stretched Nb_3Sn phase, $E^{tot}_{\mathrm{Nb/Nb_3Sn}}$ is the total internal energy of the relaxed Nb/Nb_3Sn system containing an interface; this was done for four different orientations. The calculated values of the interfacial internal energies at 0 K are summarized in table 4. Nb_3Sn(002)//Nb$(1\bar{1}2)$ with Orientation A has the lowest interfacial internal energy and Nb_3Sn(210)//Nb(110) with Orientation A has the largest interfacial internal energy. We note that the interfaces with Sn-deficient Nb_3Sn for all four orientations have 11%–12% smaller interfacial internal energies than those with the exact Nb_3Sn stoichiometry, table 4. In the

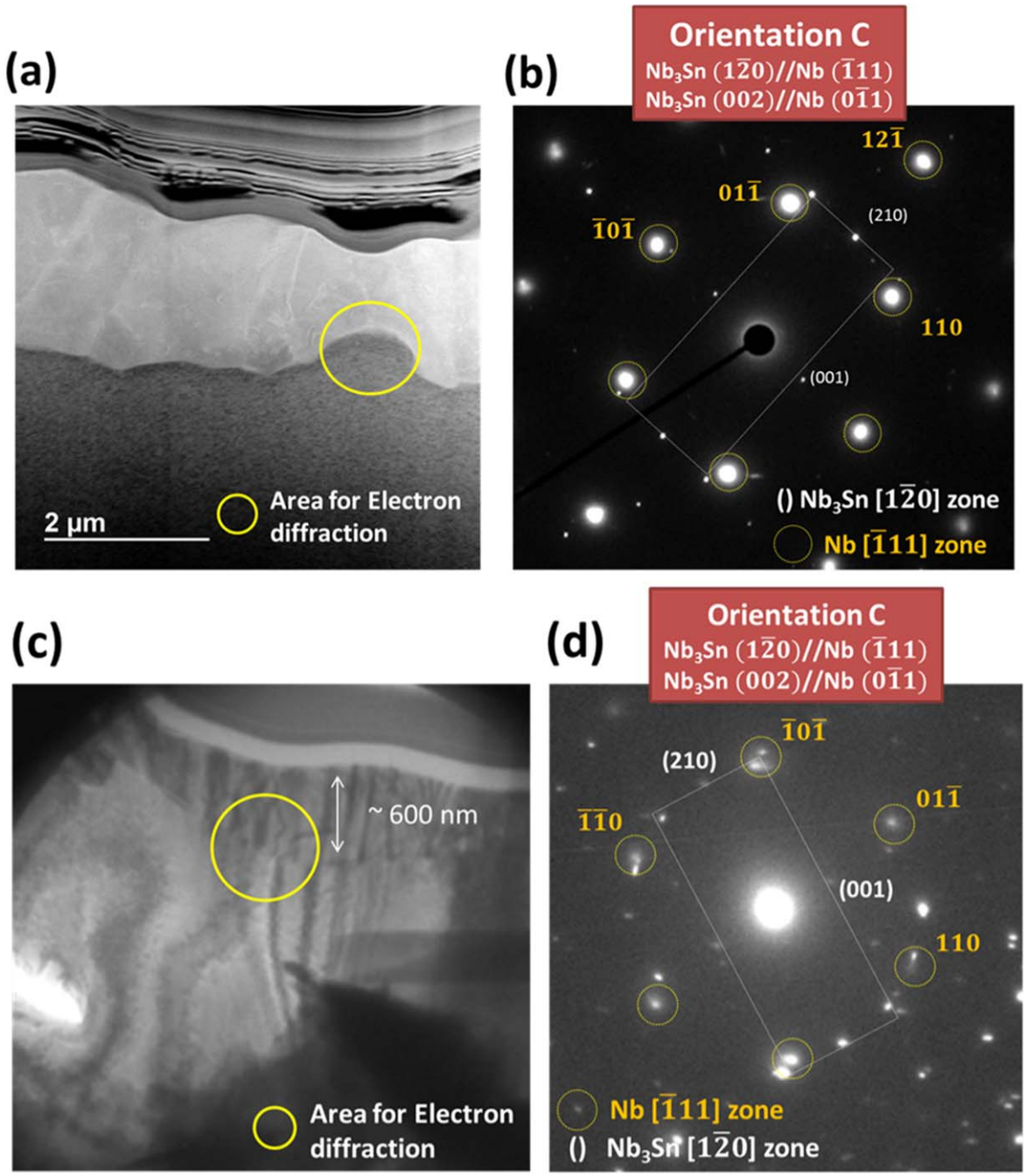

Figure 12. (a) HAADF-STEM image and (b) electron diffraction pattern of the relatively thinner Nb_3Sn grain (~700 nm) compared to other neighboring grains (~2 μm) in a good performing SRF cavity similar to ERL 1-4. (c) BF-TEM image of a thin-grain from the performance-degraded region of ERL 1-5 Nb_3Sn cavity, and (d) corresponding electron diffraction pattern. Both Nb_3Sn films were prepared at Cornell University.

early nucleation stage, the change of the bulk internal energy is negligible and Nb_3Sn nucleates readily in regions with a small interfacial internal energy. This reflects the fact that the nucleated Nb_3Sn, figure 2, is Sn-deficient and there is a large amount of nucleated Sn-deficient Nb_3Sn existing at Nb_3Sn/Nb heterophase interfaces in a Nb_3Sn layer in our experiments, figures 4, 7 and 9.

Once the Sn-deficient Nb_3Sn phase is nucleated and grows at Nb_3Sn/Nb heterophase interfaces, Sn-deficient Nb_3Sn transforms to stoichiometric Nb_3Sn by replacing Nb antisite atoms with Sn. Diffusion of Sn within a Nb_3Sn grain is slow due to the highly correlated diffusion of Sn in this ordered structure [26, 34, 50]. We note that the diffusion coefficient of Sn in Nb_3Sn is approximately three orders of magnitude smaller than even that of Nb at 1100 °C and the root mean square diffusion distance of Sn in Nb_3Sn is ~100 nm in one hour at 1100 °C [50, 54]. As a consequence, a coating time of 3.5 h is insufficient to allow Sn-deficient regions to achieve the equilibrium concentration of 25 at% Sn, if the size of the Sn-deficient regions is more than ~350 nm.

Based on our observations and prior studies [15, 19, 35], we propose a scheme for the growth of normal Nb_3Sn grains on Nb that is summarized in figure 11. At the nucleation step, figure 11, Sn vapor condenses on the Nb surface forming Sn nucleation sites for Nb_3Sn embryos, which become stable Nb_3Sn nuclei that eventually become Nb_3Sn grains. According to the phase diagram, first-principles calculations, and STEM-EDS results, the Nb_3Sn nuclei are likely to be Sn-deficient, see figures 1, 2 and table 4. When the temperature is increased to 1100 °C, significant grain growth of Nb_3Sn occurs [15] and the lateral growth of Nb_3Sn results in impingement and coalescence of Nb_3Sn grains, which result in grain boundaries [55]. Once Nb_3Sn covers completely the Nb substrate, the growth of the Nb_3Sn coating is controlled by an interfacial reaction at the Nb_3Sn/Nb heterophase interface and is limited by the diffusion of Sn along the grain boundaries, that is, short-circuit diffusion. In this case, there could be Sn-deficient regions in the middle of grains resulting from slow Sn diffusion in Nb_3Sn, which is highly correlated.

4.5. Correlation between microstructure and superconductivity of Nb_3Sn SRF cavities

Trenikhina *et al* [14] describe a study in which a direct correlation was made between the degradation of the Q_0 of an SRF cavity (Q versus E curve of ERL 1-5 in figure 1) and thin grains in the regions of degraded performance. We reexamined one of the coupons from a region with degraded performance and analyzed one of the thin grains for ORs. It also exhibited Orientation C as demonstrated using electron diffraction, figures 12(c), (d), which provides additional strong evidence that the degradation of superconductivity in a Nb_3Sn cavity is due to thin grains, which is caused by specific ORs of Nb_3Sn/Nb associated with small net Sn-fluxes. Therefore, a critical net Sn flux is required to avoid the formation of thin grains with Orientation C. Also, pre-anodization of Nb substrates, which introduces 70–100 nm niobium oxide layers on Nb, is employed to induce homogeneous nucleation of Nb_3Sn embryos at a high number density, which significantly reduces the large lateral growth of the thin grains with Orientation C, figures 12(a), (b) [15, 35]. Indeed, the grain with Orientation C found in the Nb_3Sn coating on pre-anodized Nb is similar in grain size ($\sim 2\ \mu$m) to other neighboring grains, figures 12(a), (b). Furthermore, the cavity with the grain with Orientation C exhibits no degradation of superconductivity until 17 MV m^{-1}, similar to ERL 1-4 in figure 1(a). This demonstrates that even though grains with Orientation C may be present in a Nb_3Sn coating, the detrimental effects of thin grains on SRF cavity performance can be mitigated by controlling the Sn flux and inducing homogeneous nucleation of Nb_3Sn embryos using pre-anodization of Nb substrates. It is possible that Nb oxide layers on the surface may interfere with the epitaxial growth of Nb_3Sn on Nb, causing more randomly oriented and more chemically uniform Nb_3Sn coatings.

The effect of Sn-deficient Nb_3Sn on the superconductivity of Nb_3Sn SRF cavity is anticipated to be unfavorable because the T_c of Sn-deficient Nb_3Sn (17 at% Sn) decreases from 18.3 K of perfect Nb_3Sn to 6 K, which is less than the T_c of Nb (9.2 K). The distribution of Sn-deficient regions in the Nb_3Sn coatings and detailed correlations between Sn-deficient regions and SRF cavity performance require additional in-depth studies.

5. Conclusions

Nb_3Sn coatings on Nb prepared by a vapor-diffusion process for SRF cavity applications were analyzed systematically using TEM, EBSD and first-principles calculations.

- Four types of ORs between Nb_3Sn and Nb (Orientations A, B, C and D) were detected and analyzed by electron diffraction and HR-STEM. Notably, there is a close relationship between the formation of thin grains in low Sn-flux regions and the ORs, Nb_3Sn $(1\bar{2}0)//Nb$ $(\bar{1}11)$ and Nb_3Sn $(002)//Nb$ $(0\bar{1}1)$, termed Orientation C. Orientation C displays a large lattice mismatch (12.3%) between Nb_3Sn (002) and Nb $(0\bar{1}1)$ and a high density of misfit dislocations as observed employing HR-STEM images.
- The formation of abnormally thin grains is attributed to the slow migration of the Nb_3Sn/Nb heterophase interface with Orientation C, caused by its high density of misfit dislocations.
- The formation of Sn-deficient regions at the heterophase interfaces were also quantified employing first-principle calculations. We found that heterophase interfaces with Sn-deficient Nb_3Sn have smaller interfacial internal energies than those with perfect Nb_3Sn.
- In the early nucleation stage, the new phase with a small interfacial free energy nucleates readily when the change of the bulk internal energy is small, which results in large areas of Sn-deficient Nb_3Sn existing in the Nb_3Sn layer as experimentally demonstrated.
- The Nb_3Sn/Nb heterophase interfaces and the crystallographic ORs of Nb_3Sn with Nb play important roles in the formation of abnormal thin grains and Sn-deficient regions, imperfections that are detrimental to the superconducting properties of Nb_3Sn SRF cavities.
- The current study may yield new possibilities for controlling the imperfections in Nb_3Sn coatings and improving their quality to increase the accelerating electric field of Nb_3Sn cavities.

Acknowledgments

We are grateful to Drs Amir R Farkoosh, Xuefeng Zhou, and Sung-Il Baik, and Mr Qingqiang Ren for valuable discussions. We also thank Professors James P Sethna, Thomas Arias and David A Müller for valuable discussions and suggestions. This research is supported by the United States Department of Energy, Offices of High Energy. Fermilab is operated by the Fermi Research Alliance LLC under Contract No. DE-AC02-07CH11359 with the United States Department of Energy. This work made use of the EPIC, Keck-II, and/or SPID facilities of Northwestern University's NU*ANCE* Center, which received

support from the Soft and Hybrid Nanotechnology Experimental (SHyNE) Resource (NSF ECCS-1542205); the MRSEC program (NSF DMR-1121262) at the Materials Research Center; the International Institute for Nanotechnology (IIN); the Keck Foundation; and the State of Illinois, through the IIN. Cornell's Nb_3Sn coating program is supported by United States Department of Energy grant DE-SC0008431. NUCAPT received support from the MRSEC program (NSF DMR-1720139) at the Materials Research Center, the SHyNE Resource (NSF ECCS-1542205), and the Initiative for Sustainability and Energy (ISEN) at Northwestern University.

ORCID iDs

Jaeyel Lee https://orcid.org/0000-0001-8542-9612

References

[1] Godeke A 2006 A review of the properties of Nb_3Sn and their variation with A15 composition, morphology and strain state *Supercond. Sci. Technol.* **19** R68
[2] Arnolds G and Proch D 1977 Measurement on a Nb_3Sn structure for linear accelerator application *IEEE Trans. Magn.* **13** 500–3
[3] Hillenbrand B, Martens H, Pfister H, Schnitzke K and Uzel Y 1977 Superconducting Nb_3Sn cavities with high microwave qualities *IEEE Trans. Magn.* **13** 491–5
[4] Kneisel P, Stoltz O and Halbritter J 1979 Measurements of superconducting Nb_3Sn cavities in the GHz range *IEEE Trans. Magn.* **15** 21–4
[5] Padamsee H 2009 *RF Superconductivity: Science, Technology and Applications.* (Hoboken, NJ: Wiley)
[6] Boussard D and Linnecar T P R 1999 The LHC superconducting RF system *LHC Project Report* No. 316 (CERN)
[7] Posen S *et al* 2016 Efficient expulsion of magnetic flux in superconducting radiofrequency cavities for high Q_0 applications *J. Appl. Phys.* **119** 213903
[8] Posen S and Liepe M 2014 Advances in development of Nb_3Sn superconducting radio-frequency cavities *Phys. Rev. Spec. Top.-Accel. Beams* **17** 112001
[9] Posen S and Hall D 2017 Nb_3Sn superconducting radiofrequency cavities: fabrication, results, properties, and prospects *Supercond. Sci. Technol.* **30** 033004
[10] Posen S 2015 Understanding and overcoming limitation mechanisms in Nb_3Sn superconducting RF cavities *PhD Dissertation* Cornell University
[11] Transtrum M K, Catelani G and Sethna J P 2011 Superheating field of superconductors within Ginzburg–Landau theory *Phys. Rev.* B **83** 094505
[12] Liarte D B, Posen S, Transtrum M K, Catelani G, Liepe M and Sethna J P 2017 Theoretical estimates of maximum fields in superconducting resonant radio frequency cavities: stability theory, disorder, and laminates *Supercond. Sci. Technol.* **30** 033002
[13] Posen S, Valles N and Liepe M 2015 Radio frequency magnetic field limits of Nb and Nb_3Sn *Phys. Rev. Lett.* **115** 047001
[14] Trenikhina Y *et al* 2017 Performance-defining properties of Nb_3Sn coating in SRF cavities *Supercond. Sci. Technol.* **31** 015004
[15] Hall D L 2017 New insights into the limitations on the efficiency and achievable gradients in Nb_3Sn SRF cavities *PhD Dissertation* Cornell University
[16] Hillenbrand B, Uzel Y and Schnitzke K 1980 On the preparation of Nb_3Sn-layers on monocrystalline Nb-substrates *Appl. Phys.* **23** 237–40
[17] Pudasaini U, Eremeev G, Reece C E, Tuggle J and Kelley M 2018 Insights into formation of Nb_3Sn Film during the vapor diffusion process *18th Int. Conf. on RF Superconductivity (SRF'17) (Lanzhou, China, 17–21 July, 2017)*
[18] Becker C *et al* 2015 Analysis of Nb_3Sn surface layers for superconducting radio frequency cavity applications *Appl. Phys. Lett.* **106** 082602
[19] Stimmell J B 1978 Microwave superconductivity of Nb_3Sn *PhD Dissertation* Cornell University
[20] Charlesworth J, Macphail I and Madsen P 1970 Experimental work on the niobium-tin constitution diagram and related studies *J. Mater. Sci.* **5** 580–603
[21] Farrell H, Gilmer G and Suenaga M 1975 Diffusion mechanisms for the growth of Nb_3Sn intermetallic layers *Thin Solid Films* **25** 253–64
[22] Farrell H, Gilmer G and Suenaga M 1974 Grain boundary diffusion and growth of intermetallic layers: Nb_3Sn *J. Appl. Phys.* **45** 4025–35
[23] Suenaga M and Jansen W 1983 Chemical compositions at and near the grain boundaries in bronze-processed superconducting Nb_3Sn *Appl. Phys. Lett.* **43** 791–3
[24] Suenaga M, Luhman T and Sampson W 1974 Effects of heat treatment and doping with Zr on the superconducting critical current densities of multifilamentary Nb_3Sn wires *J. Appl. Phys.* **45** 4049–53
[25] Xu X and Sumption M D 2016 A model for the compositions of non-stoichiometric intermediate phases formed by diffusion reactions, and its application to Nb_3Sn superconductors *Sci. Rep.* **6** 19096
[26] Laurila T, Vuorinen V, Kumar A and Paul A 2010 Diffusion and growth mechanism of Nb_3Sn superconductor grown by bronze technique *Appl. Phys. Lett.* **96** 231910
[27] Xu X 2017 A review and prospects for Nb_3Sn superconductor development *Supercond. Sci. Technol.* **30** 093001
[28] Hillenbrand B, Martens H, Pfister H, Schnitzke K and Ziegler G 1975 Superconducting Nb_3Sn-cavities *IEEE Trans. Magn.* **11** 420–2
[29] Saur E and Wurm J 1962 Präparation und Supraleitungseigenschaften von Niobdrahtproben mit Nb_3Sn-Überzug *Naturwissenschaften* **49** 127–8
[30] Kresse G and Hafner J 1993 *Ab initio* molecular dynamics for liquid metals *Phys. Rev.* B **47** 558
[31] Kresse G and Furthmüller J 1996 Efficient iterative schemes for *ab initio* total-energy calculations using a plane-wave basis set *Phys. Rev.* B **54** 11169
[32] Kresse G and Furthmüller J 1996 Efficiency of ab-initio total energy calculations for metals and semiconductors using a plane-wave basis set *Comput. Mater. Sci.* **6** 15–50
[33] Straumanis M and Zyszczynski S 1970 Lattice parameters, thermal expansion coefficients and densities of Nb, and of solid solutions Nb–O and Nb–N–O and their defect structure *J. Appl. Crystallogr.* **3** 1–6
[34] Welch D, Dienes G, Lazareth O Jr and Hatcher R 1984 Defects and diffusion mechanisms in Nb_3Sn *J. Phys. Chem. Solids* **45** 1225–42
[35] Hall D, Kaufman J, Liepe M and Maniscalco J 2016 Surface analysis studies of Nb_3Sn thin films *7th Int. Particle Accelerator Conf. (IPAC'16) (Busan, Korea, 8–13 May, 2016)*
[36] Devantay H, Jorda J L, Decroux M, Muller J and Flükiger R 1981 The physical and structural properties of superconducting A15-type Nb–Sn alloys *J. Mater. Sci.* **16** 2145–53

[37] King H 1966 Quantitative size-factors for metallic solid solutions *J. Mater. Sci.* **1** 79–90
[38] Freysoldt C *et al* 2014 First-principles calculations for point defects in solids *Rev. Mod. Phys.* **86** 253
[39] Booth-Morrison C, Mao Z, Noebe R D and Seidman D N 2008 Chromium and tantalum site substitution patterns in Ni_3Al ($L1_2$) γ'-precipitates *Appl. Phys. Lett.* **93** 033103
[40] Hesse D 1997 The submicroscopic structure of reaction fronts in solid–solid reactions and its correlation with reaction mechanism and kinetics *Solid State Ion.* **95** 1–15
[41] Sieber H, Hess D and Werner P 1997 Misfit accommodation mechanisms at moving reaction fronts during topotaxial spinel-forming thin-film solid-state reactions: a high-resolution transmission electron microscopy study of five spinels of different misfits *Phil. Mag.* A **75** 889–908
[42] Beckers M, Schell N, Martins R, Mücklich A and Möller W 2005 The influence of the growth rate on the preferred orientation of magnetron-sputtered Ti–Al–N thin films studied by *in situ* x-ray diffraction *J. Appl. Phys.* **98** 044901
[43] Carter G 2000 Preferred orientation in thin film growth—the survival of the fastest model *Vacuum* **56** 87–93
[44] Hofmann S *et al* 2008 Ledge-flow-controlled catalyst interface dynamics during Si nanowire growth *Nat. Mater.* **7** 372
[45] Gorla C, Mayo W, Liang S and Lu Y 2000 Structure and interface-controlled growth kinetics of $ZnAl_2O_4$ formed at the $(11\bar{2}0)$ ZnO/$(01\bar{1}2)$ Al_2O_3 interface *J. Appl. Phys.* **87** 3736–43
[46] Hesse D, Werner P, Mattheis R and Heydenreich J 1993 Interfacial reaction barriers during thin-film solid-state reactions: the crystallographic origin of kinetic barriers at the $NiSi_2$/Si (111) interface *Appl. Phys.* A **57** 415–25
[47] Li C *et al* 2016 The structure of a propagating $MgAl_2O_4$/MgO interface: linked atomic- and μm-scale mechanisms of interface motion *Phil. Mag.* **96** 2488–503
[48] Sieber H, Werner P and Hesse D 1997 The atomic structure of the reaction front as a function of the kinetic regime of a spinel-forming solid-state reaction *Phil. Mag.* A **75** 909–24
[49] Nandasiri M *et al* 2011 Influence of growth rate on the epitaxial orientation and crystalline quality of CeO_2 thin films grown on Al_2O_3 (0001) *J. Appl. Phys.* **109** 013525
[50] Besson R, Guyot S and Legris A 2007 Atomic-scale study of diffusion in A15 Nb_3Sn *Phys. Rev.* B **75** 054105
[51] Clouet E, Nastar M and Sigli C 2004 Nucleation of Al_3Zr and Al_3Sc in aluminum alloys: from kinetic Monte Carlo simulations to classical theory *Phys. Rev.* B **69** 064109
[52] Mao Z, Chen W, Seidman D and Wolverton C 2011 First-principles study of the nucleation and stability of ordered precipitates in ternary Al–Sc–Li alloys *Acta Mater.* **59** 3012–23
[53] Ratke L and Voorhees P W 2013 *Growth and Coarsening: Ostwald Ripening in Material Processing* (Berlin: Springer Science & Business Media)
[54] Müller H and Schneider T 2008 Heat treatment of Nb_3Sn conductors *Cryogenics* **48** 323–30
[55] Thompson C V 2000 Structure evolution during processing of polycrystalline films *Annu. Rev. Mater. Sci.* **30** 159–90